Defect complexes in congruent LiNbO₃ and their optical signatures

Yanlu Li

State Key Laboratory of Crystal Materials, Shandong University, 250100 Jinan, China

W. G. Schmidt and S. Sanna[*]

Lehrstuhl für Theoretische Physik, Universität Paderborn, 33095 Paderborn, Germany

The structure and stability of defect clusters in LiNbO₃, as well as their influence on the linear and nonlinear optical susceptibilities, are calculated within density functional theory (DFT) using semilocal and hybrid exchange-correlation functionals. In particular, the complexes modeling the Li shortage during the crystal growth, the Li-vacancy model and the Nb-vacancy model, are examined in detail. It is found that clustering significantly decreases the formation energies of all considered defects with respect to the dilute limit. The Li-vacancy model is energetically preferred with respect to the total formation energy, while the Nb-vacancy model has the lowest formation energy per single point defect. The independent-particle approximation based on the hybrid DFT electronic structure describes the LiNbO₃ optical response much better than semilocal DFT. A further improvement between the calculated optical absorption and second-harmonic generation spectra with experiment is achieved if the calculations take defect complexes into account. Nb antisite polarons give rise to optical absorption within the band gap.

PACS number(s): 61.72.J−, 61.66.Fn, 78.20.−e

I. INTRODUCTION

Ferroelectric lithium niobate (LiNbO₃) possesses a series of outstanding properties, such as high electro-optic coefficients, high optical transparency in the near-infrared wavelengths, high Curie temperature, and large nonlinear coefficients [1–5]. It has therefore been the material of choice for a large number of optical applications, such as electro-optic modulators, Q-switching, optical parametric oscillation, second-harmonic generation, and surface acoustic wave devices [6,7]. Generally, Li deficient LiNbO₃ crystals with congruent composition ([Li]/[Nb] ≈ 0.94) grown by the Czochralski technique are used in optical and acoustic devices [3,8]. In order to maintain overall charge neutrality, the Li deficiency causes the formation of further defects for charge compensation. Thus the nonstoichiometry in congruent samples results in a large number of intrinsic point defects and defect complexes, far beyond concentrations typically realized by doping. While the defect complexes are known to strongly modify the material's properties, e.g., the optical response [9,10], their detailed compositions and atomic structures are largely unclear.

Three defect models have been proposed to describe the shortage of Li during the growth [11–14]: lithium vacancies charge compensated by an oxygen vacancy ($2V_{Li}^- + V_O^{2+}$, O-vacancy model), and niobium antisites compensated by either niobium vacancies ($5Nb_{Li}^{4+} + 4V_{Nb}^{5-}$, Nb-vacancy model) or lithium vacancies ($Nb_{Li}^{4+} + 4V_{Li}^-$, Li-vacancy model). The O-vacancy model has been discarded, as the formation of oxygen vacancies in LiNbO₃ is energetically unfavorable [12–14]. On the contrary, the Li deficiency has been shown to result in an increase of the Nb concentration, leading to the formation of a large number of Nb_{Li} antisites, whose existence was repeatedly proved by structural studies [12–14]. The latter, being fourfold positively charged, require charge compensation by Li or Nb vacancies. The experimental determination of the precise defect configurations is complicated due to the complexity of the ternary material as well as hindered by the fact that most of the conceivable defect positions share the same C_3 symmetry. Theoretical work by Donnerberg *et al.* [15] as well as Xu *et al.* [16] finds the Li-vacancy model to be energetically more favorable than the Nb-vacancy model. Recent calculations for single intrinsic LiNbO₃ point defects [17] indicate that—depending on the preparation conditions—Nb antisites, Li vacancies, and Nb vacancies may coexist in lithium niobate.

Little is known on defect clustering effects. Xu *et al.* [18] proposed a configuration for the Li-vacancy model in which four lithium vacancies are located at the nearest-neighbor (NN) sites around the niobium antisite. This arrangement is found to be energetically more favorable than Kim's model [19] where the niobium antisite is surrounded by three NN lithium vacancies and one additional lithium vacancy shifted along the z direction. There is no generally accepted structure that describes the Nb-vacancy model. Mixed models where both Li and Nb vacancies compensate for the antisite were studied by Xu *et al.* [18].

Almost all calculations of the LiNbO₃ optical response, e.g., Refs. [20–23], are performed for the stoichiometric material, which is rarely used for applications. Riefer and two of the present authors recently studied the influence of point defects on the LiNbO₃ optical response and concluded that both the Li-vacancy model and the Nb-vacancy model may account for part of the differences between the measured optical response of congruent lithium niobate samples and the spectra calculated for the stoichiometric material [5]. In that work, however, the Li- and Nb-vacancy models were approximated by a random arrangement of single point defects and clustering effects were neglected.

The present work aims at a better understanding of (i) the interaction between intrinsic LiNbO₃ point defects and (ii) their influence on the material's optical response. Therefore density-functional theory calculations are performed on the geometries, formation energies, and cohesive energies of three charge-compensated defect complex models,

*Corresponding author: simone.sanna@uni-paderborn.de

namely $5\mathrm{Nb}_{\mathrm{Li}}^{4+} + 4\mathrm{V}_{\mathrm{Nb}}^{5-}$ (Nb-vacancy model), $\mathrm{Nb}_{\mathrm{Li}}^{4+} + 4\mathrm{V}_{\mathrm{Li}}^{-}$ (Li-vacancy model), and $2\mathrm{Nb}_{\mathrm{Li}}^{4+} + 3\mathrm{V}_{\mathrm{Li}}^{-} + \mathrm{V}_{\mathrm{Nb}}^{5-}$ (mixed model). Subsequently, the influence of the defect complexes on the electronic properties, the frequency-dependent dielectric function, and the second-order polarizability tensor of LiNbO$_3$ are investigated.

II. METHODOLOGY

The present calculations employ the Vienna *ab initio* Simulation Package (VASP) [24,25] implementation of DFT in conjunction with the projector-augmented-wave (PAW) formalism [26]. Thereby the Li $2s^1$, Nb $4p^6\,5s^1\,4d^4$, and O $2s^2\,2p^4$ states are treated as valence electrons. The electronic wave functions are expanded in plane waves using an energy cutoff of 400 eV. Hexagonal $3\times2\times2$ supercells containing 540 atoms are used to model defect complexes. The Perdew-Burke-Ernzerhof (PBE) functional [27] is used to model the electron exchange and correlation (XC) within the generalized gradient approximation (GGA). Hybrid DFT calculations were performed for test purposes using hexagonal $2\times2\times1$ 120 atom supercells containing modeling isolated Nb antisites $\mathrm{Nb}_{\mathrm{Li}}$, Li vacancies V_{Li}, and Nb vacancies V_{Nb}. Thereby, we use the Hyde-Scuseria-Ernzerhof (HSE06) functional [28,29], where 25% Hartree-Fock exchange is included for short-range interactions. Structural relaxation is performed using 0.01 eV/Å as the force convergence criterion. The Brillouin zones of the 120 and 540 atom supercells are sampled with a $4\times4\times4$ ($2\times2\times2$ for hybrid DFT) Monkhorst-Pack mesh [30] and the Γ point, respectively.

The defect formation energies of a defect X with charge q is dependent on the Fermi level position and is calculated as [31,32]

$$E_f(X^q) = E^{\mathrm{total}}(X^q) - E^{\mathrm{total}}(\mathrm{bulk}) + \sum_i n_i \mu_i$$
$$+ q(E_F + E_v + \Delta V), \qquad (1)$$

where $E^{\mathrm{total}}(X^q)$ is the total energy derived from a supercell with defect X, $E^{\mathrm{total}}(\mathrm{bulk})$ is the total energy of the defect-free supercell, n_i indicates the number of atoms of species i that have been added or removed upon defect creation, and μ_i are the corresponding chemical potentials. E_F is the Fermi level with respect to the bulk valence band maximum E_v, and ΔV aligns the reference potential in the defect supercell with that in the bulk [31]. The chemical potentials μ_i depend on the preparation conditions; see, e.g., Ref. [33]. In the following we assume Nb-rich conditions (line CE in Fig. 2 in Ref. [17]), consistent with the Li-deficient composition of congruent samples as well as earlier calculations [17]. The cohesive energy of the complex $X_1 X_2 \ldots X_n$, i.e., the energy necessary to separate it into single defects X_1, X_2, ..., X_n, is obtained from the formation energies

$$E_c[(X_1 \ldots X_n)^q] = E_f[(X_1 \ldots X_n)^q] - \sum_1^n E_f(X_n^{q_n}), \quad (2)$$

where $q = q_1 + q_2 + \cdots + q_n$. A negative cohesive energy corresponds to a stable complex.

To assess the defect energetics at finite temperatures, the free energy $F = E - TS$ rather than the total energy E should be considered. The electronic entropy, negligible here due

to the large LiNbO$_3$ band gap, the lattice vibrations, and the configuration entropy contribute to F. The configuration contribution may be expected to be the most important in the present context, where structures with largely different numbers and configurations of point defects need to be compared. It is calculated in this work according to Boltzmann's entropy formula

$$S = k_B \ln W, \qquad (3)$$

where k_B is the Boltzmann constant, and W is the number of defect cluster configurations in the LiNbO$_3$ lattice. W is approximated here by multiplying the possible combinations of each defect type building the cluster. Considering the largest used 540-atom supercell, containing 108 Li, 108 Nb, and 324 oxygen atoms, the W are calculated with the binomial coefficients C_n^k as

$$W(\mathrm{Nb}_{\mathrm{Li}} + 4\mathrm{V}_{\mathrm{Li}}) = C_{108}^1 C_{107}^4,$$
$$W(5\mathrm{Nb}_{\mathrm{Li}} + 4\mathrm{V}_{\mathrm{Nb}}) = C_{108}^5 C_{108}^4,$$
$$W(2\mathrm{Nb}_{\mathrm{Li}} + \mathrm{V}_{\mathrm{Nb}} + 3\mathrm{V}_{\mathrm{Li}}) = C_{108}^2 C_{108}^1 C_{106}^3,$$

and result in configurational entropy values of 0.0017, 0.0027, and 0.0022 eV/K, respectively. The largest entropic contribution to the free energy value is calculated for the $5\mathrm{Nb}_{\mathrm{Li}}^{4+} + 4\mathrm{V}_{\mathrm{Nb}}^{5-}$ complex in the 540-atom cell: There it amounts to about 0.8 eV at room temperature, which is still considerably smaller than the cluster formation energy of 14.23 eV.

The periodic boundary conditions applied here cause interactions between the defect and its periodic images [32,34–38]. These artificial interactions represent a major issue in the simulation of isolated defects. The corresponding error can be minimized by charge correction schemes or by an extrapolation to infinite cell dimensions as described in Ref. [17]. The situation is different, however, if defect clusters modeling the congruent crystal compositions are investigated. Our 540-atom cells model a Li deficiency of 3.7 mol %, which is a realistic representation of the Li shortage of congruent crystals. While strain effects can be considered negligible in our large cells, the electrostatic interactions between periodic images mirror real interactions between the defect clusters in congruent samples. Nonetheless, in order to estimate the magnitude of the electrostatic interactions, we have calculated the formation and binding energy for a test system, the $\mathrm{Nb}_{\mathrm{Li}}^{4+}$-$\mathrm{V}_{\mathrm{Li}}^{-}$ defect pair, as a function of the defect-defect distance for supercells of various size containing from 120 to 540 atoms. The largest energy deviation amounts to 0.08 eV, which can be considered an upper limit of the error bar in our calculations.

Based on the relaxed atomic structures obtained for the various defects considered here, the dielectric function $\varepsilon(\omega)$ as well as the second-harmonic generation (SHG) tensor $\chi^{(2)}_{\alpha\beta\gamma}(\omega)$ in dependence on the photon energies $\hbar\omega$ is obtained. These calculations are performed within the independent-particle approximation [39–41] based on the electronic structure obtained within DFT-GGA or hybrid DFT. The SHG coefficients are obtained from the two- and three-band contributions according to Refs. [42–44] using the implementation by Riefer *et al.* [5]. All valence and conduction states within 30 and 25 eV, respectively, from the valence band maximum are included in the calculations. The Brillouin zone sampling has been done
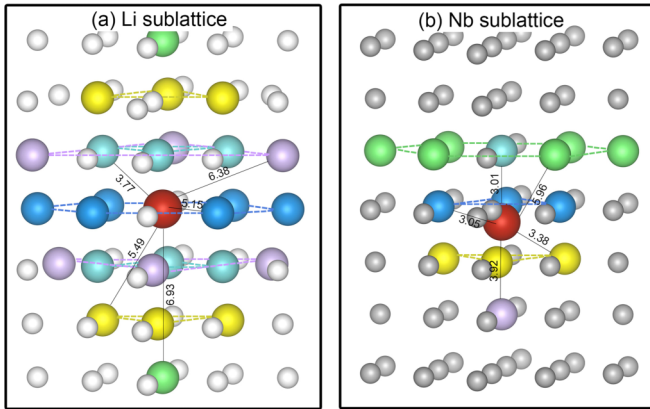
FIG. 1. (Color online) Nearest-neighbor (NN) sites to Nb_{Li}^{4+} in the Li (a) and Nb (b) sublattices of LiNbO₃. Large light blue, dark blue, yellow, violet, and green balls indicate the 1NN, 2NN, 3NN, 4NN, and 5NN sites. Distances are given in Å. Small white and gray balls represent Li and Nb atoms, respectively.
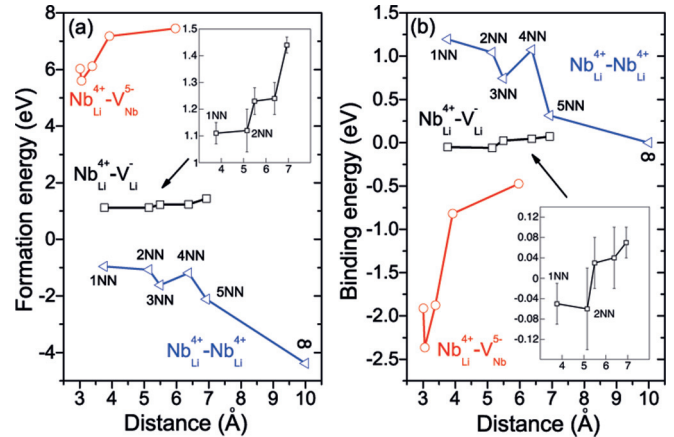

FIG. 2. (Color online) Calculated formation energies (a) and binding energies (b) of defect pairs in dependence on their distance. The calculated error bars are shown in the inset. The Fermi energy is assumed to correspond to the valence band maximum.

with $6 \times 6 \times 6$ and $4 \times 4 \times 4$ **k**-point meshes and the Γ point, respectively, for LiNbO₃ bulk calculations as well as 120 and 540 atom cells.

III. RESULTS AND DISCUSSION

A. Structures and energetics

The large number of defect cluster configurations does not allow for a complete energy comparison of all conceivable structural models. Therefore we proceed step by step, starting with a niobium antisite and add subsequently further defects, each in the respective lattice position that minimizes the cluster formation energy. This procedure clearly is not guaranteed to result in the global energy minimum, but in fact yields cluster configurations that are lower in energy than previously suggested models.

The niobium antisite and lithium vacancy lie on the Li sublattice, while the niobium vacancy is on the Nb sublattice. Thus, in first approximation, the cationic sublattice is relevant for the charge compensation mechanisms. In Fig. 1 the nearest-neighbor (NN), second-nearest-neighbor (2NN), third-nearest-neighbor (3NN), fourth-nearest-neighbor (4NN), and fifth-nearest-neighbor (5NN) sites to a niobium antisite in the Li and Nb sublattices of lithium niobate are shown. It can be seen that the niobium antisite has 6 (1) equivalent NN sites, 6 (3) equivalent 2NN sites, and 6 (3) equivalent 3NN sites on the Li (Nb) sublattice. The difference is due to the fact that the niobium antisite belongs to the Li sublattice, the vertical shift of which with respect to the Nb sublattice reduces the number of the equivalent neighboring sites.

1. Defect pairs

The distance-dependent formation and binding energy of Nb_{Li}^{4+}-V_{Nb}^{5-}, Nb_{Li}^{4+}-V_{Li}^{-}, and Nb_{Li}^{4+}-Nb_{Li}^{4+} pairs is shown in Fig. 2. The respective charge states of these defects are the most stable ones for the majority of Fermi-level positions [17].

The Nb_{Li}^{4+} antisite bonds to a V_{Li}^{-} at its NN and 2NN sites as a stable complex due to their negative binding energies (black line). In particular, a V_{Li}^{-} at the 2NN site has the lowest

formation energy (1.1 eV) and highest (negative) binding energy of all Nb_{Li}^{4+}-V_{Li}^{-} pairs. The binding energy of Nb_{Li}^{4+}-V_{Li}^{-} pairs beyond the 2NN shell is within the estimated error bar of our calculations.

The Nb_{Li}^{4+}-V_{Nb}^{5-} pairs have the highest formation energies (larger than 5 eV) and largest (negative) binding energies among the defect pairs considered here. The high formation energy is due to the large strain caused by V_{Nb}^{5-}; see Ref. [17]. The strong bonding of Nb_{Li}^{4+}-V_{Nb}^{5-} results from electrostatics, which causes an attractive interaction for all distances. The strongest bonding occurs for 2NN pairs.

Nb_{Li}^{4+} pairs, in contrast, repel each other due to their Coulomb interaction. Both the pair formation energies and the repulsion decrease with distance. Values labeled by ∞ represent the limiting case of isolated defects. Considering isolated Nb_{Li}^{4+} defects, no clustering should be expected. This may change, however, due to the attractive interaction caused by additional V_{Li}^{-} or V_{Nb}^{5-} defects, as will be investigated below.

2. Cluster models

Charge-compensated clusters are set up here defect by defect starting from a Nb_{Li}^{4+}-V_{Li}^{-} or Nb_{Li}^{4+}-V_{Nb}^{5-} pair. Further defects are then subsequently added, each in the position that minimizes the formation energy. Taking the Li-vacancy model as an example, we first put V_{Li}^{-} at the NN and 2NN sites of Nb_{Li}^{4+}, since they have similar formation and binding energies. Additional V_{Li}^{-} defects are used to probe the energetics of the remaining NN and 2NN sites to find the most stable $Nb_{Li}^{4+} + 4V_{Li}^{-}$ cluster configuration. 3NN and 4NN vacancies are not considered due to their small binding energy (see Fig. 2). In the case of $5Nb_{Li}^{4+} + 4V_{Nb}^{5-}$ and $2Nb_{Li}^{4+} + V_{Nb}^{5-} + 3V_{Li}^{-}$ models, where more than one Nb_{Li}^{4+} occurs, all NN sites of all Nb_{Li}^{4+} defects were examined. The most stable configurations found this way for the Nb-vacancy model ($5Nb_{Li}^{4+} + 4V_{Nb}^{5-}$), the Li-vacancy model ($Nb_{Li}^{4+} + 4V_{Li}^{-}$), and the mixed $2Nb_{Li}^{4+} + V_{Nb}^{5-} + 3V_{Li}^{-}$ model are shown in Fig. 3.

In case of the energetically favored $Nb_{Li}^{4+} + 4V_{Li}^{-}$ complex found here, one V_{Li}^{-} is located at the Nb_{Li}^{4+} NN, and the

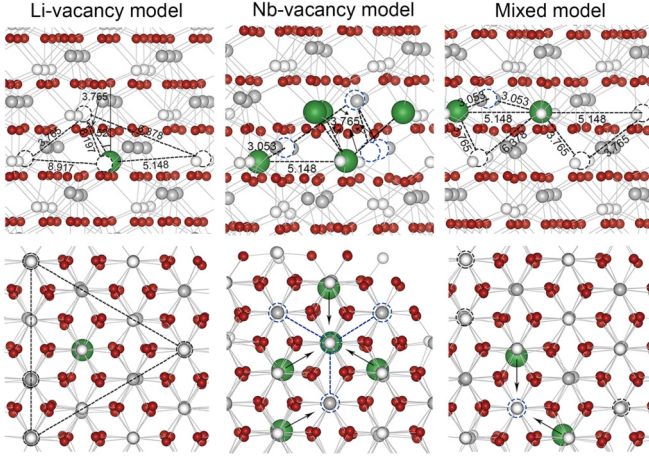Li-vacancy model   Nb-vacancy model   Mixed model

FIG. 3. (Color online) Side and top view of the energetically most favored defect complexes. Large green balls, black circles, and blue circles indicate Nb antisite, Li and Nb vacancies, respectively. Small gray, white, and red balls represent Nb, Li, and O atoms, respectively. The arrows indicate the structural relaxation.

remaining three are at 2NN sites; see Fig. 3, left-hand side. The present Li-vacancy model thus differs both from the one reported by Xu *et al.* [18], where four V_{Li}^- are located at NN sites, and also from Kim's model [19], where the niobium antisite is surrounded by three lithium vacancies in the NN positions and one lithium vacancy is separated from the cluster by a shift along the z direction. These two models from the literature were probed here for an energetic comparison. It is found that Xu's and Kim's models are 0.16 and 0.27 eV less stable than the present model, respectively, consistent with the finding of Ref. [18] that the former is 0.16 eV more stable than the latter. The present Li-vacancy model does not preserve the crystal C_3 symmetry, due to the V_{Li}^- at the NN site, which leads to a small nonaxial polarization component. However, averaging over many microscopic cluster configurations, the

polarization components orthogonal to the bulk polarization will vanish for finite samples.

Three Nb_{Li}^{4+} of the present $5Nb_{Li}^{4+} + 4V_{Nb}^{5-}$ complex are located at the Nb_{Li}^{4+} NN sites, while one Nb_{Li}^{4+} is at the 2NN site; cf. Fig. 3, middle. The four V_{Nb}^{5-} thus occupy the NN and 2NN sites of the same Nb_{Li}^{4+}. This is different from the model of Ref. [16], where four Nb_{Li}^{4+} as well as the four V_{Nb}^{5-} are at the NN sites of the same Nb_{Li}^{4+}.

Since Nb vacancies are expected for specific preparation conditions [17], we also study one model where the antisite-induced charge imbalance is partially compensated by Li vacancies as well as by Nb vacancies. The energetically most stable configuration modeling this situation is shown in Fig. 3, right-hand side. Due to the electrostatic repulsion between V_{Li}^- and V_{Nb}^{5-}, it is rather extended. Also, it breaks the crystal symmetry and is characterized by a large lattice deformation.

3. Defect energetics

The formation energies of the defect complexes calculated here are compared with previous findings in Table I. In the case of systems that are not fully charge compensated the formation energies depend on the Fermi level position E_F within the band gap. As one might expect, the formation energy of the cluster increases generally with increasing number of point defects constituting the complex: In terms of the total formation energy, the Nb_{Li}^{4+} charge compensated by $4V_{Li}^-$ is more favorable than $5V_{Nb}^{5-}$ compensated by $4V_{Nb}^{5-}$. The energy of the neutral cluster of $2Nb_{Li}^{4+}$, $3V_{Li}^-$, and V_{Nb}^{5-} lies in between. The energetic ordering of the clusters as well as of the single defects calculated here agrees with previous findings [13,16,45,46]. The specific formation energies are quite different, however. This does not only hold for shell model and empirical potential calculations, but also for previous DFT results [16] that predict a negative formation energy for the Li-vacancy model, see Table I, in contrast to the present findings. This difference may be related to the different cell size or cluster configuration.

TABLE I. Calculated defect formation energies E_f and cohesive energies E_c (in eV) for various defect complexes under Nb-rich condition, compared with previous calculations. E_f^{dilute} indicates the formation energy in the dilute solution limit. E_F denotes the Fermi level position in the band gap.

| Defect	E_f	E_f^{dilute}	E_c	E_f (E_f^{dilute}) in Ref.
$Nb_{Li}^{4+} + V_{Li}^-$	$1.12 + 3E_F$	$4.65 + 3E_F$	-3.53	
$Nb_{Li}^{4+} + 2V_{Li}^-$	$3.58 + 2E_F$	$7.61 + 2E_F$	-4.03	
$Nb_{Li}^{4+} + 3V_{Li}^-$	$6.17 + E_F$	$10.57 + E_F$	-4.40	
$Nb_{Li}^{4+} + 4V_{Li}^-$	8.76	13.53	-4.77	-4.90 (-6.50) [PAW-GGA] [16,18]
$Nb_{Li}^{4+} + V_{Nb}^{5-}$	$5.60 - E_F$	$12.16 - E_F$	-6.56	
$2Nb_{Li}^{4+} + V_{Nb}^{5-}$	$2.75 + 3E_F$	$13.86 + 3E_F$	-11.11	
$2Nb_{Li}^{4+} + 2V_{Nb}^{5-}$	$9.92 - 2E_F$	$24.32 - 2E_F$	-14.40	
$3Nb_{Li}^{4+} + 2V_{Nb}^{5-}$	$7.69 + 2E_F$	$26.02 + 2E_F$	-18.33	
$3Nb_{Li}^{4+} + 3V_{Nb}^{5-}$	$13.76 - 3E_F$	$36.48 - 3E_F$	-22.72	
$4Nb_{Li}^{4+} + 3V_{Nb}^{5-}$	$10.81 + E_F$	$38.18 + E_F$	-27.37	
$4Nb_{Li}^{4+} + 4V_{Nb}^{5-}$	$18.14 - 4E_F$	$48.64 - 4E_F$	-30.50	
$5Nb_{Li}^{4+} + 4V_{Nb}^{5-}$	14.23	50.34	-36.11	18.27 [PAW-GGA] [16]
$2Nb_{Li}^{4+} + V_{Nb}^{5-} + V_{Li}^-$	$5.03 + 2E_F$	$16.82 + 2E_F$	-11.79	
$2Nb_{Li}^{4+} + V_{Nb}^{5-} + 2V_{Li}^-$	$7.46 + E_F$	$19.77 + E_F$	-12.31	
$2Nb_{Li}^{4+} + V_{Nb}^{5-} + 3V_{Li}^-$	10.01	22.73	-12.72	
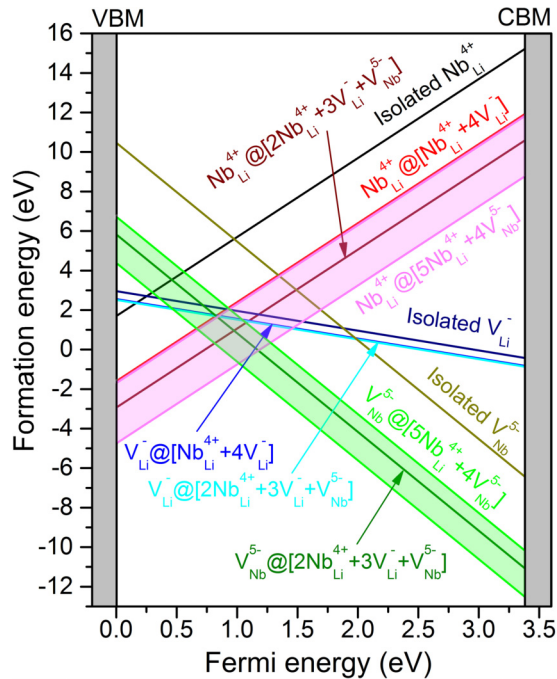
FIG. 4. (Color online) Formation energies of single defects Nb_{Li}^{4+}, V_{Li}^-, and V_{Nb}^{5-} in the bulk and in the corresponding defect complexes as a function of Fermi energy. Equivalent lattice sites in the crystal bulk may become nonequivalent within a defect cluster, resulting in lattice-site-dependent formation energies. The shaded regions indicate the corresponding formation energy range.

The cluster formation energies calculated here are considerably lower than the sum of the formation energies of the respective isolated constituents. The energy difference is the cluster cohesive energy, which amounts to 4.77 eV and 36.11 eV in the case of the Li- and Nb-vacancy model, respectively. Similarly to the formation energy, the cohesive energy grows with the number of single defects that constitute the complex. Therefore, the Nb-vacancy model has the largest cohesive energy.

A meaningful stability criterion is given by the comparison of the formation energy of single point defects within a defect complex and in the dilute limit. The respective values for Nb_{Li}^{4+}, V_{Li}^-, and V_{Nb}^{5-} defects in the three investigated defect complexes and in the dilute limit are shown in Fig. 4. All the defects considered here have lower formation energy within the complex in comparison to the isolated case. The energy gain for V_{Li}^- amounts to 0.4 eV in both the Li-vacancy model and in the mixed model. Far larger energy gains of more than 3 eV are realized for both Nb_{Li}^{4+} and V_{Nb}^{5-} when they are formed within the Nb-vacancy model and in the mixed model. This reflects the high cohesive energies shown in Table I. These large energy gains are on the one hand due to the Coulomb attraction between oppositely charged point defects within the cluster, and, on the other hand, due to favorable lattice relaxation. In the vast majority of LiNbO₃ samples the Fermi energy lies within the lower half of the fundamental band gap. As can be seen in Fig. 4, for low values of the electron chemical potential the calculated antisite Nb_{Li}^{4+} formation energy is

negative, i.e., the formation of antisites is favorable, in accord with the experimental findings for congruent LiNbO₃.

However, a word of caution is in order when interpreting the defect energies calculated here. In particular the use of a semilocal XC functional limits the predictive power of the calculations: Hybrid DFT calculations are expected to decrease the formation energy for Nb_{Li}^{4+} by about 7 eV, and increase it by about 1 and 4 eV for V_{Li}^- and V_{Nb}^{5-}, respectively [17]. Using smaller 120-atom supercells modeling the charge compensation by Li vacancies, we have verified that the changes predicted for isolated defects are roughly transferable to the defect complexes, where they cancel out to a large extent. Nevertheless, the use of hybrid DFT—presently not applicable to large defect clusters—will obviously modify the calculated energies, at least quantitatively.

B. Defect states and optical response

The lithium niobate electronic bands below and above the fundamental band gap are determined by O $2p$ and Nb $4d$ states. The corresponding densities of states (DOS) for stoichiometric LiNbO₃ (SLN) as well as single point defects and defect clusters considered here are shown in Fig. 5. Compared to the ideal crystal, V_{Li}^-, but in particular Nb_{Li}^{4+} and V_{Nb}^{5-}, gives rise to a downshift of Nb $4d$ states below the bulk conduction band minimum (CBM). At the same time, the density of O $2p$ at the valence band maximum is reduced. Again, this effect is most pronounced for Nb_{Li}^{4+}. Only by changing the charge state of the Nb antisite, i.e., formation of small polarons Nb_{Li}^{3+} or bipolarons Nb_{Li}^{2+}, additional states are introduced in the upper half of the fundamental band gap. Note that the latter calculations, shown in Fig. 5(c), are performed within hybrid DFT, in order to describe the localization of the polaron and bipolaron states correctly. Therefore the employed 120-atom supercells mirror higher defect concentrations. The DOS signatures of single point defects also show up in the modification of the electronic properties of the charge-compensated defect models studied here. A downshift of states at the CBM is observed that is most pronounced for the mixed and the Nb-vacancy model. These two models also give rise to the strongest DOS depletion at the VBM. Generally, a peak broadening occurs for the defect complexes in comparison to the ideal material (in gray in Fig. 5).

The defect implications on the LiNbO₃ linear optical response are shown in Fig. 6. Experimentally, lithium niobate shows two main absorption bands, at around 5 and 9 eV [47]. These features are reproduced by DFT calculations, at energies that are about 2 eV lower, however. The inclusion of quasiparticle effects within the *GW* approximation and electron-hole attraction as well as local-field effects has been shown to result in an excellent agreement between measured and calculated data [5,20]. Such many-body perturbation theory (MBPT) calculations, however, are presently out of reach for the supercell sizes considered here. Therefore the present calculations are performed within the independent-particle approximation, based on either the DFT-GGA or the hybrid DFT electronic structure. From the comparison of the GGA and hybrid DFT bulk spectra with experiment shown in the upper panel of Fig. 6, one sees that the latter corrects at
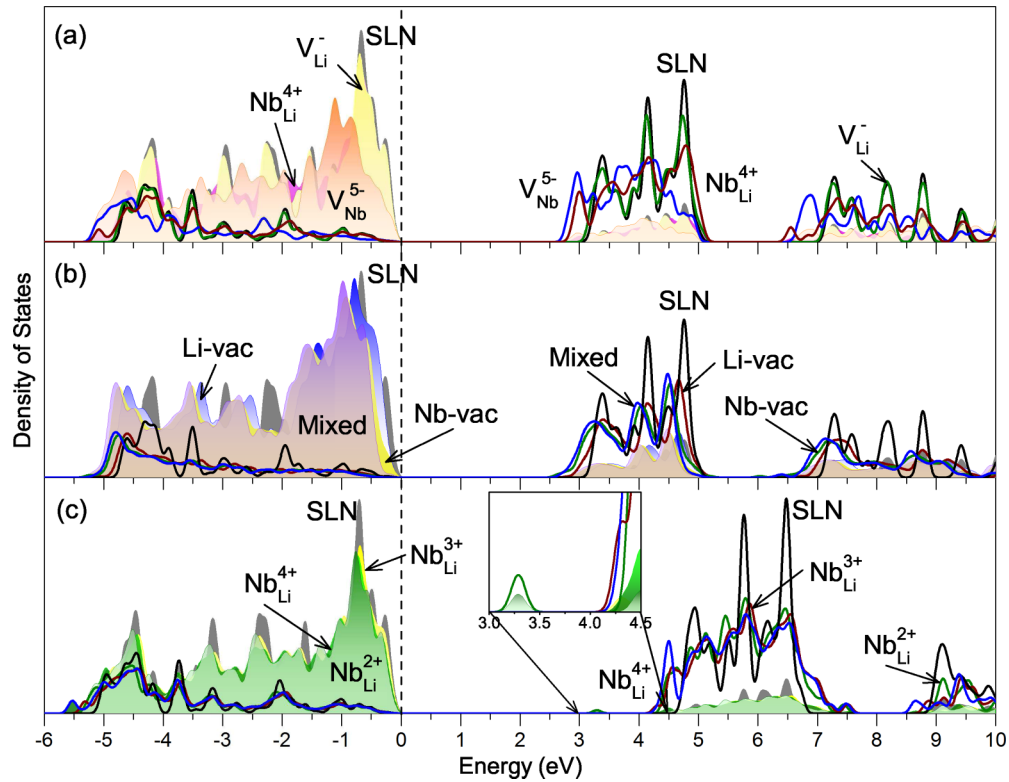
FIG. 5. (Color online) Calculated LiNbO$_3$ density of states projected on O 2p (shadows) and Nb 4d (lines). DFT-GGA calculations for single point defects and defect complexes are shown in (a) and (b), while hybrid DFT calculations for Nb antisite polarons are shown in (c).
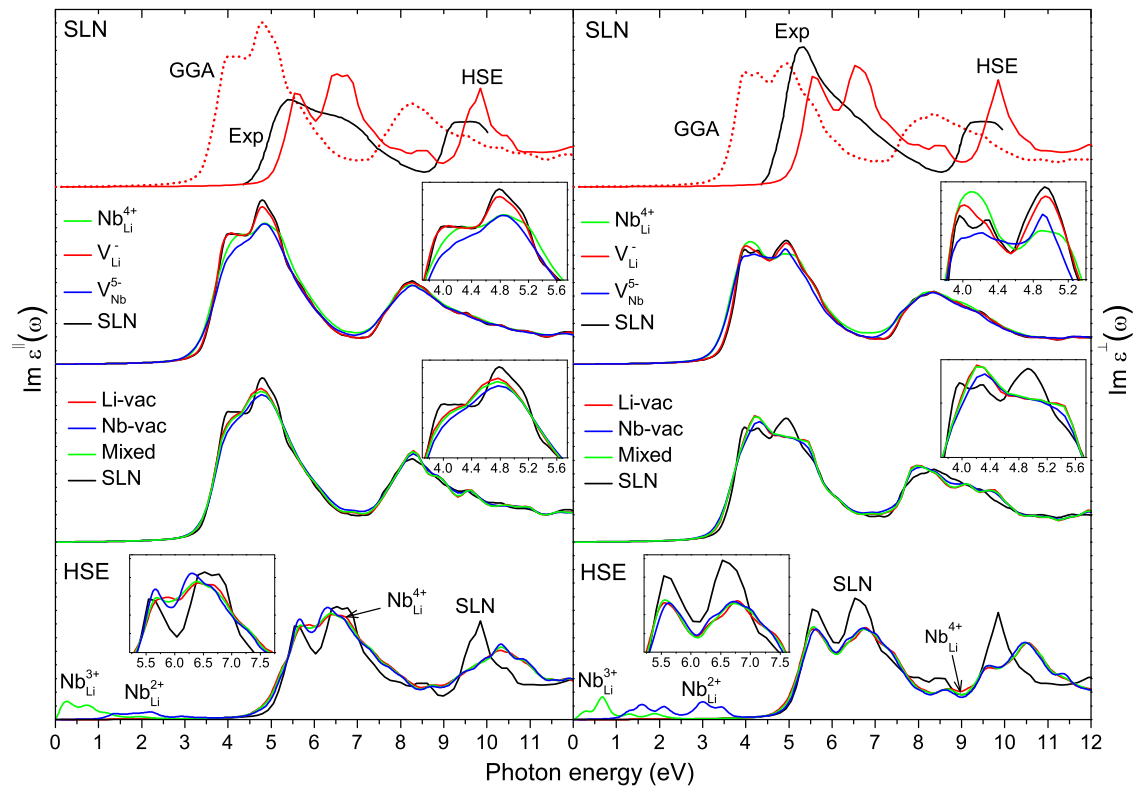

FIG. 6. (Color online) Calculated extraordinary (left) and ordinary (right) optical absorption for bulk LiNbO$_3$ as well as single defects and defect complexes in comparison with experimental data [47]. The calculations were performed within the independent-particle approximation based on either the DFT-GGA or the hybrid DFT electronic structure, as indicated.

least one shortcoming of the former: The calculated adsorption features are blueshifted and now agree with experiment within about 0.5 eV. On the other hand, a sharpening of the peak structure occurs. This holds in particular for the high-energy absorption feature that arises from transitions between O $2p$ valence states and conduction states above 9 eV, but also for first shoulder close to the absorption onset. The fact that similar line shape changes are observed in MBPT calculations [5] suggests that they are not simply artifacts due to the hybrid DFT applied here. On the other hand, experimentally no peak splitting in the first absorption band occurs, and also the high-energy feature is broader than calculated here. Since the experiments are done for congruent material, while the calculations refer to stoichiometric lithium niobate, the differences might be related to material defects.

In order to address this possibility we explore the influence of single point defects as well as defect complexes on the optical absorption. Since the modeling of defect complexes requires large 540-atom supercells, the calculations are performed using DFT-GGA. As can be seen in Fig. 6, the optical absorption of LiNbO₃ is barely affected by V_{Li}^-, while Nb_{Li}^{4+} and in particular V_{Nb}^{5-} wash out the double-peak structure of the first absorption band, most notably for $\varepsilon^\parallel$, smooth the second absorption feature, and lead to a redshift of the optical excitation energies of the order of 0.2 eV, especially for $\varepsilon^\perp$. In order to better understand the respective influence of lattice deformations and electronic structure modification due to point defects on the optical response, we performed additional calculations for single defects. The Nb_{Li}^{4+} point defect creation without lattice relaxation gives rise to Nb $4d$ states close to the VBM that shift in response to the lattice relaxation close to the CBM. The optical transitions from the host valence band to the Nb $4d$ defect states are thus shifted from about 0.5 eV for the frozen lattice to the first absorption peak at about 4 eV for the structurally relaxed defect. Here they add oscillator strength to the spectrum, which leads in the case of $\varepsilon^\perp$ to a reversal of the respective height of the two features constituting the first double peak. For the other point defects, in particular for V_{Nb}^{5-}, it is found that electronic and structural effects on the optical response intertwine in a similar way.

The point defect signatures can still be recognized in the optical response calculated for charge-compensated congruent crystals: Since V_{Nb}^{5-} most strongly influences the optical response, the calculations for the Nb-vacancy model yield stronger differences to the stoichiometric LiNbO₃ data than the calculations for the Li-vacancy model and the mixed model. The disappearance of the double-peak structure in particular is most notable in the case of the Nb-vacancy model. The results obtained here for the optical response of energy-minimized charge compensation models are very similar to previous calculations [5], where deviations from the stoichiometric composition were modeled with a random arrangement of point defects. Obviously, the mutual interaction of the point defects within the defect cluster has little influence on the total optical response, at least for the defects studied here. Overall, all models representing the congruent composition change the absorption of the stoichiometric material in a similar way: We find a small redshift of the optical absorption accompanied by a smoothening of the absorption fine structure. Given that both

the hybrid DFT data presented here as well as earlier MBPT calculations [5] differ from the experiment by means of (i) a small blueshift of a few tenths of one eV and (ii) a fine structure not resolved experimentally, this indicates that the neglect of point defects at least partially accounts for the discrepancies between simulations and measurements. However, at this point one has to be cautious, as many-body effects not considered here may strongly affect localized defect electronic states.

The lithium niobate optical response may also be influenced by small polarons and bipolarons, i.e., electrons trapped at Nb_{Li}^{4+} [17,48,49]. We calculated their optical absorption using hybrid DFT, in order to describe the localized electronic states more realistically than within semilocal XC functionals. The results are shown in the lower panel of Fig. 6. Compared to the ideal bulk spectrum, the onset of the main optical absorption band is redshifted by about 0.2 eV, both for Nb_{Li}^{4+} as well as for the small polaron Nb_{Li}^{3+} and the bipolaron Nb_{Li}^{2+}. The former finding simply confirms our DFT-GGA results discussed above. This redshift is related to defect-induced empty states at about 0.2 eV below the CBM that can be seen in the DOS shown in Fig. 5(a). If one electron is trapped at Nb_{Li}^{4+}, the corresponding state is lowered in energy by about 0.5 eV; see Fig. 5(c). The transitions from this defect state to the conduction band give rise to optical absorption for photon energies up to about 2.5 eV for the small polaron. If another electron is trapped, a small bipolaron forms, that is characterized by strong structural relaxation [50]. This causes a further downshift of the defect states [cf. Fig. 5(c)] that now gives rise to optical absorption for photon energies between about 1 and 3.5 eV, i.e., blueshifted with respect to the small polaron absorption.

Finally, we investigated the defect influence on the second-harmonic generation (SHG) coefficients. The calculated 31 and 33 components (real parts) of the SHG tensor are compared with the available experimental data [6,51–58] in Fig. 7. Thereby $\chi_{\alpha\beta\gamma}^{(2)}(\omega)$ spectra were calculated for the stoichiometric material as well as for single point defects and congruent crystal models. The calculations were done within DFT-GGA, and, in the case of stoichiometric LiNbO₃, within hybrid DFT. The latter spectra are blueshifted by about 0.8 eV and show an overall lower intensity, in particular for the 33 component. Considering first the stoichiometric LiNbO₃ calculations, the hybrid DFT values are much closer to the experimental data than the DFT-GGA results. This is particularly evident for the 33 component. However, while using hybrid DFT considerably reduces the calculated optical nonlinearities, they are still larger than most of the measured values. Again, defects could be a possible explanation. Indeed, similar to the calculated linear absorption spectra, single point defects, in particular Nb_{Li}^{4+} and V_{Nb}^{5-}, broaden the spectral signatures and reduce the signal strength. This trend is suitable to improve the agreement between the calculated and the measured nonlinearities. In particular the 33 component calculated for photon energies of about 1 eV, where a number of experimental data are available, gets much closer to the experimental value when assuming the Nb-vacancy model rather than stoichiometric crystals for the calculation. However, this seemingly good agreement should not be overrated: On the one hand, excitonic effects neglected here are expected to influence the SHG spectra [44].
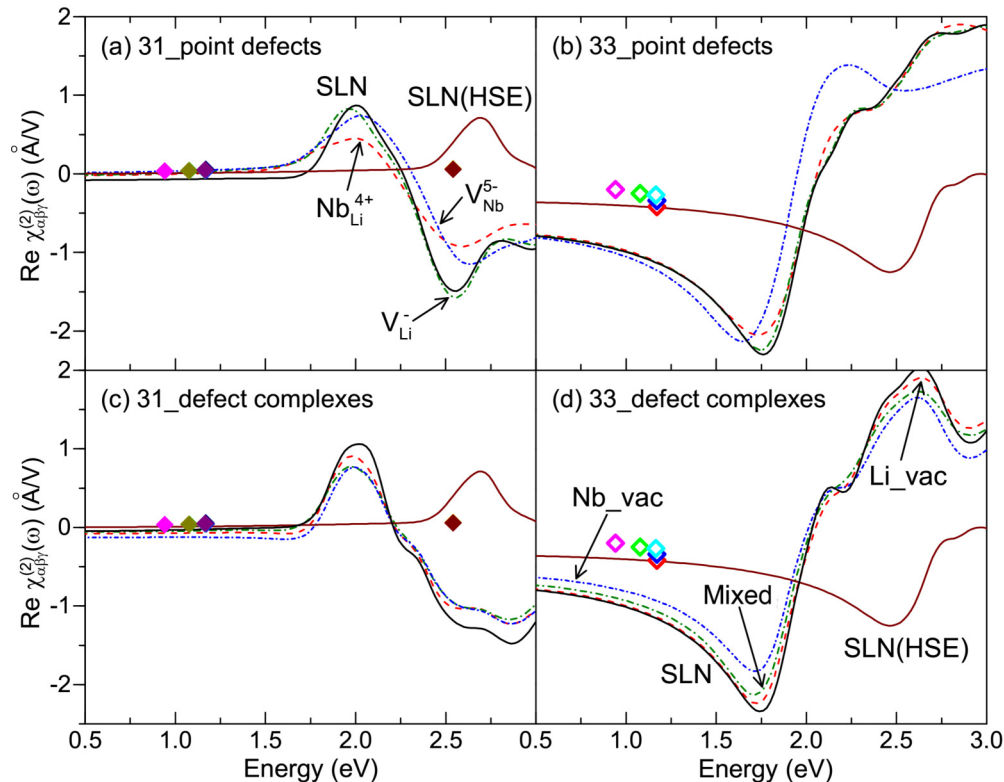
FIG. 7. (Color online) Calculated 31 and 33 $\chi^{(2)}(\omega)$ tensor components for bulk $LiNbO_3$ as well as single defects and defect complexes in comparison with experimental data [6,51–58]. The calculations were performed within DFT-GGA or hybrid DFT, as indicated.

On the other hand, experimental data covering a larger energy window rather than single frequencies are required for a really conclusive and meaningful experiment-theory comparison.

IV. CONCLUSIONS

Semilocal as well as hybrid DFT calculations were performed in order to determine the structure and energetics as well as the optical properties of single point defects and defect complexes in lithium niobate. Clustering effects are found to considerably reduce the formation energies of intrinsic $LiNbO_3$ point defects. In particular the energy required to form Nb antisite and Nb vacancies within charge-compensated defect complexes is reduced by several electronvolts. From the cluster defect formation energies calculated here we expect a variety of charge compensation mechanisms rather than a single specific configuration to occur in congruent lithium niobate samples. The calculation of linear and nonlinear optical response functions within hybrid DFT leads to a notably better agreement with the measured data than corresponding calculations within DFT-GGA. A further improvement between simulation and experiment can be expected from the extrapolation of the GGA calculations for defect complexes to the hybrid DFT electronic structure: Generally, the point defects lead to a broadening of the spectral signatures and reduce the sign strength, both for the linear and SHG spectra. This holds in particular for Nb vacancies. Small polarons and bipolarons trapped at Nb antisite defects give rise to electronic states in the lithium niobate fundamental gap and cause optical absorption for low-energy photons.

[1] J. G. Bergman, A. Ashkin, A. A. Ballman, J. M. Dziedzic, H. J. Levinstein, and R. G. Smith, Appl. Phys. Lett. **12**, 92 (1968).

[2] E. H. Turner, F. R. Nash, and P. M. Bridenbaugh, J. Appl. Phys. **41**, 5278 (1970).

[3] V. Gopalan, V. Dierolf, and D. A. Scrymgeour, Annu. Rev. Mater. Res. **37**, 449 (2007).

[4] F. Luedtke, K. Buse, and B. Sturman, Phys. Rev. Lett. **109**, 026603 (2012).

[5] A. Riefer, S. Sanna, A. Schindlmayr, and W. G. Schmidt, Phys. Rev. B **87**, 195208 (2013).

[6] G. D. Boyd, K. Nassau, R. C. Miller, W. L. Bond, and A. Savage, Appl. Phys. Lett. **5**, 234 (1964).

[7] F. S. Chen, J. Appl. Phys. **40**, 3389 (1969).

[8] F. P. Safaryan, R. S. Feigelson, and A. M. Petrosyan, J. Appl. Phys. **85**, 8079 (1999).

[9] I. V. Kityk, M. Makowska-Janusik, M. D. Fontana, M. Aillerie, and F. Abdi, J. Phys. Chem. B **105**, 12242 (2001).

[10] I. V. Kityk, M. Makowska-Janusik, M. D. Fontana, M. Aillerie, and F. Abdi, J. Appl. Phys. **90**, 5542 (2001).

[11] D. M. Smyth, Prog. Solid State Chem. **15**, 145 (1984).

[12] S. C. Abrahams and P. Marsh, Acta Crystallogr., Sect. B **42**, 61 (1986).

[13] H. Donnerberg, S. M. Tomlinson, C. R. A. Catlow, and O. F. Schirmer, Phys. Rev. B **40**, 11909 (1989).

[14] N. Iyi, K. Kitamura, F. Izumi, J. K. Yamamoto, T. Hayashi, H. Asano, and S. Kimura, J. Solid State Chem. **101**, 340 (1992).

[15] H. Donnerberg, S. M. Tomlinson, C. R. A. Catlow, and O. F. Schirmer, Phys. Rev. B **44**, 4877 (1991).

[16] H. Xu, D. Lee, J. He, S. B. Sinnott, V. Gopalan, V. Dierolf, and S. R. Phillpot, Phys. Rev. B **78**, 174103 (2008).

[17] Y. Li, W. G. Schmidt, and S. Sanna, Phys. Rev. B **89**, 094111 (2014).

[18] H. Xu, D. Lee, S. B. Sinnott, V. Dierolf, V. Gopalan, and S. R. Phillpot, J. Phys.: Condens. Matter **22**, 135002 (2010).

[19] S. Kim, V. Gopalan, K. Kitamura, and Y. Furukawa, J. Appl. Phys. **90**, 2949 (2001).

[20] W. G. Schmidt, M. Albrecht, S. Wippermann, S. Blankenburg, E. Rauls, F. Fuchs, C. Rödl, J. Furthmüller, and A. Hermann, Phys. Rev. B **77**, 035106 (2008).

[21] W. Y. Ching, Z. Q. Gu, and Y. N. Xu, Phys. Rev. B **50**, 1992 (1994).

[22] H. Akkus, S. Cabuk, and A. M. Mamedov, Int. J. Nanoelectron. Mater. **3**, 53 (2010).

[23] A. Riefer, S. Sanna, A. V. Gavrilenko, and W. G. Schmidt, IEEE Trans. Ultrason. Ferroelectr. Freq. Control **59**, 1929 (2012).

[24] G. Kresse and J. Furthmuller, Comput. Mater. Sci. **6**, 15 (1996).

[25] G. Kresse and J. Furthmuller, Phys. Rev. B **54**, 11169 (1996).

[26] G. Kresse and D. Joubert, Phys. Rev. B **59**, 1758 (1999).

[27] J. P. Perdew, K. Burke, and M. Ernzerhof, Phys. Rev. Lett. **77**, 3865 (1996).

[28] J. Heyd, G. E. Scuseria, and M. Ernzerhof, J. Chem. Phys. **118**, 8207 (2003).

[29] A. V. Krukau, A. F. Vydrov, O. A. Izmaylov, and G. E. Scuseria, J. Chem. Phys. **125**, 224106 (2006).

[30] H. J. Monkhorst and J. D. Pack, Phys. Rev. B **13**, 5188 (1976).

[31] G. C. Van de Walle and J. Neugebauer, J. Appl. Phys. **95**, 3851 (2004).

[32] S. Lany and A. Zunger, Phys. Rev. B **78**, 235104 (2008).

[33] S. Sanna and W. G. Schmidt, Phys. Rev. B **81**, 214116 (2010).

[34] P. A. Schultz, Phys. Rev. Lett. **84**, 1942 (2000).

[35] H. P. Komsa, T. T. Rantala, and A. Pasquarello, Phys. Rev. B **86**, 045112 (2012).

[36] M. Leslie and M. J. Gillan, J. Phys. C: Solid State Phys. **18**, 973 (1985).

[37] G. Makov and M. C. Payne, Phys. Rev. B **51**, 4014 (1995).

[38] C. Freysoldt, J. Neugebauer, and C. G. Van de Walle, Phys. Rev. Lett. **102**, 016402 (2009).

[39] H. Ehrenreich and M. H. Cohen, Phys. Rev. **115**, 786 (1959).

[40] S. L. Adler, Phys. Rev. **126**, 413 (1962).

[41] N. Wiser, Phys. Rev. **129**, 62 (1963).

[42] D. E. Aspnes, Phys. Rev. B **6**, 4648 (1972).

[43] J. L. P. Hughes and J. E. Sipe, Phys. Rev. B **53**, 10751 (1996).

[44] R. Leitsmann, W. G. Schmidt, P. H. Hahn, and F. Bechstedt, Phys. Rev. B **71**, 195209 (2005).

[45] Q. K. Li, B. Wang, C. H. Woo, H. Wang, and R. Wang, J. Phys. Chem. Solid **68**, 1336 (2007).

[46] R. M. Araujo, K. Lengyel, R. A. Jackson, L. Kovacs, and M. E. G. Valerio, J. Phys.: Condens. Matter **19**, 046211 (2007).

[47] E. Wiesendanger and G. Gntherodt, Solid State Commun. **14**, 303 (1974).

[48] O. F. Schirmer, M. Imlau, C. Merschjann, and B. Schoke, J. Phys.: Condens Matter **21**, 123201 (2009).

[49] H. H. Nahm and C. H. Park, Phys. Rev. B **78**, 184108 (2008).

[50] Y. Li, S. Sanna, and W. G. Schmidt, J. Chem. Phys. **140**, 234113 (2014).

[51] I. Shoji, T. Kondo, A. Kitamoto, M. Shirane, and R. Ito, J. Opt. Soc. Am. B **14**, 2268 (1997).

[52] M. M. Choy and R. L. Byer, Phys. Rev. B **14**, 1693 (1976).

[53] D. A. Kleinman and R. C. Miller, Phys. Rev. **148**, 302 (1966).

[54] R. C. Miller and A. Savage, Appl. Phys. Lett. **9**, 169 (1966).

[55] J. Bjorkholm, IEEE J. Quantum Electron. **4**, 970 (1968).

[56] W. F. Hagen and P. C. Magnante, J. Appl. Phys. **40**, 219 (1969).

[57] R. C. Miller, W. A. Nordland, and P. M. Bridenbaugh, J. Appl. Phys. **42**, 4145 (1971).

[58] B. F. Levine and C. G. Bethea, Appl. Phys. Lett. **20**, 272 (1972).